Compressive Sensing based on Optical Coding

Marko Stamenkovic
Supervisor: Dipl.-Phys. Markus Kamm

January 25, 2017

Abstract

In this work we analyze the properties and specificities of the dynamical, electrically addressed technology of *spatial light modulators*(SLM). We simulate the lens aberration correcting property in order to compare different devices (Holoeye [2]) and conclude that the GAEA (4094x2464) produces the best results. We then analyze the optical realization of the Radon transform (realized with a SLM) proposed by [4] and discarded their results due to some artificial considerations. We propose a novel generalizable implementation of the optical realization of the Radon transform as well as its inverse, we suggest a joint transform correlator setup to realize it and test the image reconstruction based on a small number of projections via compressive sensing methods. We conclude that the results are similar to some state of the art ([8] and [9]) research on the Radon transform reconstruction. In order to demonstrate the applicability of a SLM, we propose two experiments: an alternative proof of the optical Radon transform based on a 4f-correlator and a compressive sensing based system known as the *double random phase encoding*.

Contents

1 Introduction

Since the 1930's, the branch of physics known as optics has gradually developed closer ties with the communication and information sciences of electrical engineering. Both communication systems and imaging systems are designed to collect or process information. In the former case, the interest is focused on signals of temporal nature while the latter one treats spatial informations. From an abstract point of view, this difference is superficial and the strongest evidence to confirm the similarities arises from the mathematical formalism used to describe both systems: the Fourier analysis.

Lately, the exponential development of computer sciences added a third actor known as computational physics and mathematics. The possibility to simulate physical systems offers many improvements in the understanding of fundamental principles but also gives a new perspective in the field of information processing. In this context, a strong parallel has been drawn between optical and numerical processing. While both aim at solving the same problem, the two fields face different constraints. On one hand, the optical processing is able to treat continuous signals but the substantial nature of the system is subject to statistical variations and errors. On the other hand, numerical processing allows to treat error-less signals at the price of a discretization. Therefore, modern engineering focuses on translating efficient models in the other system in order to overcome their technical restrictions. This field of research has gained a lot of attention recently with a major technological improvement allowing to dynamically process optical informations: the *spatial light modulator*.

Sony, as a highly competitive actor in technology, creates bridges through modern engineering between theoretical discoveries and real-life applications. Among all the investigated fields and groups, the *Computational Imaging Group* at the *Stuttgart Technology Center* concentrates its efforts on finding adequate solutions and applications from theoretical improvements, actively contributing to modern engineering. The present work points in this direction and presents three tools or principles widely used in imaging and the possible links between them: the *spatial light modulator*, the *Radon transform* and the *compressive sensing*.

2 Spatial light modulator

Optical processing requires technologies able to gather informations rapidly, by some electronic means, one would prefer a direct interface between the electronic information and the data processing system. For this reason, the field of optical information processing has explored a wide range of devices able to convert an electronic signal into spatially modulated optical signals. Such a device is called a *spatial light modulator* and is abbreviated SLM.

There is a broad categorization of SLMs into two classes: (1) electrically driven SLMs and (2) optically driven SLMs. In the former case, electronic signals representing an information directly drive a device in such a way that they control its spatial distribution of absorption or phase shift. In the latter case, the information is imported in the form of an optical image on the SLM, rather than in electrical form. Often a given SLM technology may have two different forms, one suitable for electrical addressing and one suitable for optical addressing.

SLMs are not only used to input data to be processed but also to create spatial filters that can be modified in real time, in such a case, the SLM is placed on the back-focal plane of a Fourier transforming lens where it modifies the transmitted amplitude of the field in accord with a desired complex spatial filter.

Several technologies exist and provide a pleasant way to realize a SLM. These include liquid crystals SLMs, magneto-optic SLMs, deformable mirror SLMs, multiple-quantum-well SLMs and acousto-optic Bragg cells.

This work is exclusively centered on electrically addressed phase-only liquid crystals on silicon SLMs and will not treat the other technologies.

2.1 Phase-only Liquid Crystal on Silicon SLMs

The liquid crystal on silicon spatial light modulator is a device with nematic (vertical, parallel aligned or twisted) microdisplays cells of liquid crystal arranged on a silicon substrate. An electrical addressing circuit is formed on the silicon substrate by semiconductor technology. Each cell contains electrodes and controls its electrical potential independently. The electric field across the liquid crystal layer can be modulated pixel by pixel. This causes the liquid crystal molecules to tilt according to the electric field so that the phase of light can be modulated. A difference in the liquid crystal refractive indexes occurs in different tilt angles. Therefore, the optical path length changes and causes a difference in the phase. Only the phase of the light can be modulated to align the polarization of the incident light to the alignment direction of the liquid crystal molecules. One requirement to satisfy is that the incident light must be linearly polarized.

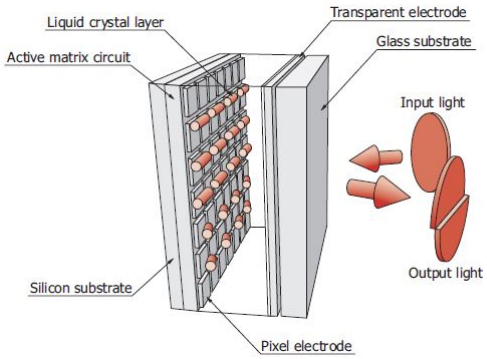

Figure 1: The liquid crystal on silicon SLM [1].

The figure 1 describes the technology of liquid crystal on silicon SLM. Several applications are possible using a phase-only spatial light modulator: beam-shaping, aberration corrections, optical pulse shaping as well as processors such as the 4f-correlator and the joint transform correlator that might be enhanced. Other applications involving imaging, projection, holography, security systems and optical tweezer are referring to this technology. A non-exhaustive list of publications can be found on the archive of the European reseller Holoeye [2]. In order to demonstrate the applicability, we simulate the lens aberration correction.

2.2 Lens aberration correction

One remarkable property of phase-only SLMs is their ability to correct undesired effects appearing when light passes through an optical system such as a single thin lens. Undesired optical effects are commonly named aberrations and several of them have been mathematically and physically described: defocus, tilt, spherical aberration, astigmatism, coma, distortion, etc. Optical aberrations are departure from the performance of an optical system from the predictions of the par-axial optics.

2.2.1 Theory

To specify the properties of a lens system, we adopt the point of view that all imaging components can be summed up into a "black box" and that the significant properties of the system can be completely described by specifying only the terminal properties of the aggregate. We assume the light passing through the entrance and exit pupil is adequately described by geometrical optics. We define z_o the distance to the object, z_i to the in-focus plane, z_a to the de-focus image point and $W(x, y)$ the path-length between the aberrations wavefront and the reference spherical wavefront. The figure 2 details the considered wavefront aberration model.

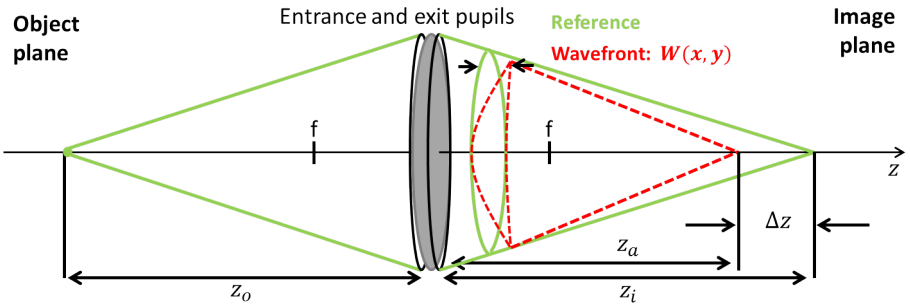

Figure 2: The wavefront aberration model.

2.2.2 Frequency Response for the Diffraction Limited Case [3]

Firstly, we introduce the aberration-free model: the diffraction limited case. Diffraction effects are resulting from the exit pupil. Let us define the amplitude transmitted by the object U_o and U_i, the image amplitude. Then:

$$U_i(u, v) = \iint_{-\infty}^{+\infty} h(u, v; \xi, \eta) U_o(\xi, \eta) d\xi d\eta \tag{1}$$

where $h(u, v; \xi, \eta)$ is the amplitude at image coordinates (u, v) in response to a point-source object at (ξ, η). In absence of aberrations, the response h represents a spherical wave sourced at z_o converging from the exit pupil toward the ideal image point z_i on the plane $(u = M\xi, v = M\eta)$, with M the magnification. The light

amplitude about the ideal image is the Fraunhofer diffraction pattern of the exit pupil, thus

$$h(u,v;\xi,\eta) = \frac{A}{\lambda z_i} \iint_{-\infty}^{+\infty} P(x,y) e^{-\frac{2\pi i}{\lambda z_i}[(u-M\xi)x+(v-M\eta)y]} dxdy \tag{2}$$

where λ is the light wavelength, (x,y) the coordinates on the exit pupil plane and $P(x,y)$ is the pupil function of the exit pupil. For a diffraction limited system, the image is the convolution of the input object with an impulse response that is the Fraunhofer diffraction pattern of the exit pupil.

A complete description of Fourier Optics has been done by J.W. Goodman [3].

2.2.3 The Generalized Pupil function

When wavefront errors exist, we consider the exit pupil is illuminated by a perfect spherical wave but that a phase-shifting plate exists in the aperture, thus deforming the wavefront that leaves the pupil. If the phase error at the point (x,y) is represented by $\frac{2\pi}{\lambda}W(x,y)$ with $W(x,y)$ the effective path-length error, the complex amplitude transmittance $\mathcal{P}(x,y)$ is given by:

$$\mathcal{P}(x,y) = P(x,y) e^{-\frac{2\pi i}{\lambda}W(x,y)}. \tag{3}$$

The complex function $\mathcal{P}$ may be referred as the generalized pupil function. According to equation (2), in order to compute the aberrations effects, we replace the pupil function P by the generalized pupil function $\mathcal{P}$.

In order to demonstrate the properties of SLMs, we consider spherical aberrations occurring when the optical system consists of a thin lens. The phase-shifting plate can be corrected by monitoring the conjugate phase on the device. We consider that the wavefront is quadratic and can be described as:

$$W(x,y) = -\pi(NA)^2(z_a - z_i)\frac{x^2+y^2}{w^2} \tag{4}$$

where $NA = \frac{f}{w}$ is the numerical aperture of the lens, w the radius of the lens and f the focal length.

The correction is realized by defining a phase-element $T(x,y)$:

$$T(x,y) = e^{\frac{2\pi i}{\lambda}W(x,y)} \tag{5}$$

Indeed, applying the convolution theorem then multiplying the generalized pupil function $\mathcal{P}$ by the optical element T, we recover the Fourier transform of the impulse response h in the diffraction limited case.

2.2.4 Simulation

The main purpose of the simulation is to conclude which SLM device is the most suitable for an experimental realization and understand their properties. All the devices are marketed by the company Holoeye Photonics AG [2].

The table 1 shows the technical specificities of the different simulated devices. The comparison requires a precise model with the different specificities taken into account. We build a model as follows :

Device	Type	Resolution	Size	Fill Factor	Max Phase shift	Pixel Pitch
GAEA	Reflective	4094x2464	15.32mmx9.22mm	0.9	3π	3.74 μm
Pluto	Reflective	1920x1080	15.36mmx8.64mm	0.93	3.9π	8.0 μm
Leto	Reflective	1920x1080	12.5mmx7.1mm	0.93	3.6π	6.4 μm
LC-2012	Transmissive	1024x768	36.9mmx27.6mm	0.58	1.8π	36 μm

Table 1: Spatial light modulators: technical specificities.

- The continuous limit is approximated by a grid of 4096x4096 pixels, every simulation has the same input and is subject to the same wavefront aberration.
- The physical size of the devices is considered as infinite, only the resolution is taken into account. As a direct consequence, our model can't distinguish between the Pluto and the Leto device. Although, considering the different pixel sizes for the two devices, we would expect different results in favor of the Leto with the smallest pitch.
- The comparison is normalized by the smallest device, different sampling rates are considered. We define a unit cell for each resolution, each physical cell of the device will be modeled by a number of pixels from the input discretization of the space. The table 2 shows the different unit cells and the resulting resolutions considered in the simulation.
- The devices square pixels imply that we can consider square devices for simplicity.
- Fill factor and undesired effects of the resolution are simulated in order to distinguish between transmissive and reflective devices. For reflective devices, we consider that the region outside the active aera of the spatial light modulator's cell induces a phase shift $e^{i\sqrt{\phi}}$ where ϕ is the desired phase shift inside the active aera, for transmissive devices, the fill factor is dominant and reduces the portion of the cell's available aera to modulate the phase of the light, blocking the rest of the light outside the active aera. The "worst case" model combines both effects but on different directions, the undesired effects are expected to be the worst. Such a configuration is very unlikely to happen on a real device; both effects would be on the same direction. The figure 3 pictures the three considered cases.
- The maximum phase-shift is not considered in the simulation because the phase-element of T from equation (5) requires a maximum phase $\phi > 2\pi$, directly related to the modulo-like property of the exponential. We can already conclude that the LC-2012 device will not be able to perfectly correct the quadratic wavefront aberrations.

Device	Resolution	Unit Cell	Simulated Resolution
GAEA	4094x2464	4x4	1024x1024
Pluto/Leto	1920x1080	9x9	576x576
LC-2012	1024x768	16x16	256x256

Table 2: Unit cells for the devices subject to comparison.

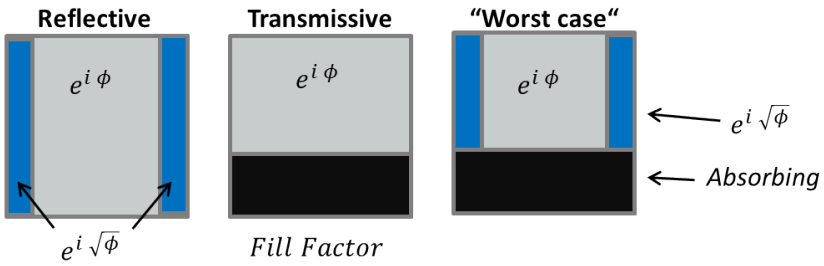

Figure 3: Model of the Unit Cell for transmissive and reflective devices.

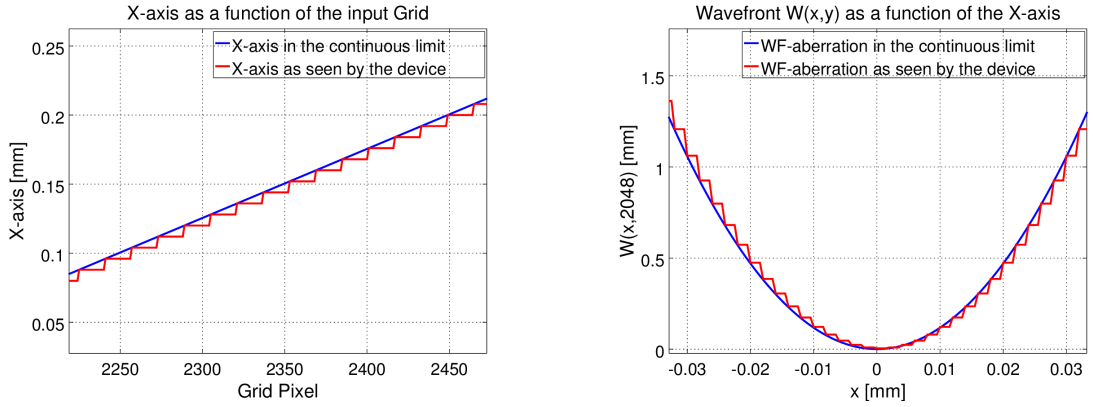

Figure 4: Comparison continuous limit/device discretization, left : x-axis, right: wavefront.

The figure 4 shows the simulation's continuous limit as seen by the devices once discretized using the unit cell definition. The continuous limit and the device discretization are compared for the x-axis and the wavefront simulation. Due to the discretization, the wavefront correction will leave artifacts in the phase shift and therefore lower the quality of the output image with respect to the diffraction limited case:

$$\mathcal{F}[h] = \mathcal{P} \times T = P \times e^{\frac{2\pi i}{\lambda}(W_{slm} - W)} = P \times e^{\frac{2\pi i}{\lambda}\Delta W} \tag{6}$$

where $\mathcal{F}[]$ is the Fourier transform operator and W_{slm} is the wavefront corrected by the simulated SLM. Since the discretization of the devices is an approximation of the continuous limit, $\Delta W \neq 0$ and some diffraction-like artifacts will appear on the output following equation (1).

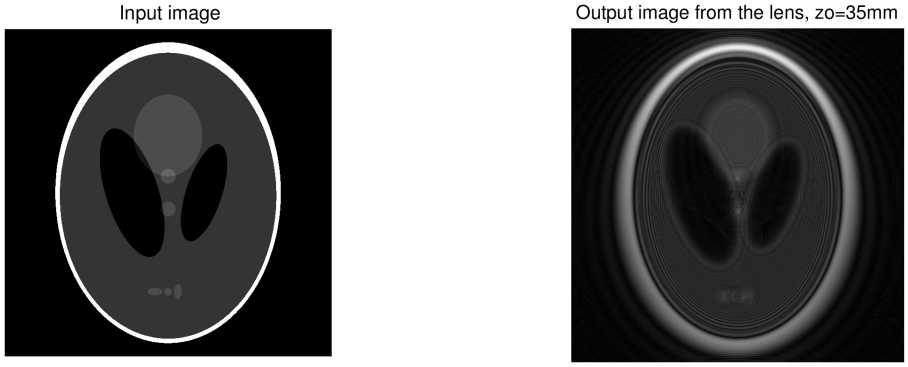

Figure 5: Simulation common to all the devices, left : input, right: lens output, $z_o = 35mm$, $z_a = 31mm$ and $f = 30mm$.

The figure 5 shows the Shepp-Logan phantom as an input and the output of the lens, considering aberrations. As expected, the effects of the wavefront is to blur the input image. Our model implies that the input and the lens output are the same for all tested devices.

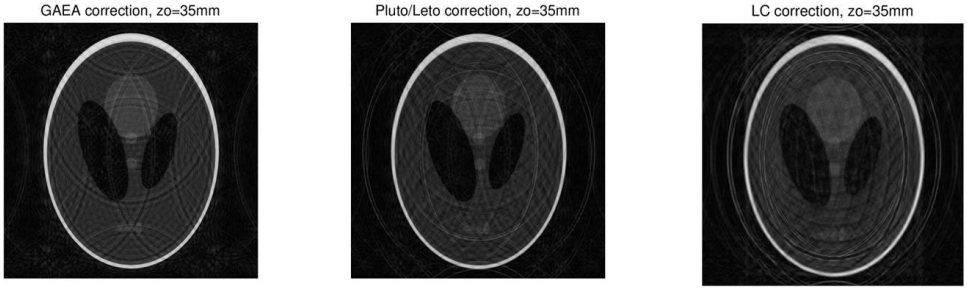

Figure 6: Wavefront corrected output, left : GAEA, middle: Pluto/Leto, right : LC-2012, $z_o = 35mm$, $z_a = 31mm$ and $f = 30mm$.

Corrected outputs are shown in figure 6. Artifacts predicted in equation (6) are present in all the figures. The simulation is also taking into account the effects of fill factor and undesired effects of the resolution. For the LC-2012 device, effects of diffraction due to low fill-factor (0.58, see Tab.1) are dominant. For the GAEA and the Pluto/Leto simulation, undesired effects of the resolution also induce a diffraction that amplifies artifacts due to the corrections themselves. In order to give an accurate comparison, we compute the correlation rate (Octave: *corr2()*) between the corrected outputs and the input.

The correlation rates for the different simulated devices are shown in the table 3. Several conclusion can be deduced. First of all, the GAEA spatial light modulator shows the best outputs and coherently satisfies the intuition "the higher resolution, the better". Furthermore, one can deduce that the reflective devices are more effi-

Device	Resolution	Corrected with discretization	Corrected with discretization + model of the unit cell	$\Delta Corr2$	Corrected with discretization + "Worst Case" model of the unit cell
GAEA	4094x2464	0.99737	0.99188	0.00549	0.96405
Pluto/Leto	1920x1080	0.99110	0.98820	0.00290	0.96370
LC-2012	1024x768	0.98339	0.85482	0.12857	0.85577

Table 3: Different correlation rates for the simulated devices.

cient than the transmissive one. This is entirely due to the generally poor fill factor for transmissive devices. Finally, looking at the difference between the correlation rates with or without undesired effects $\Delta Corr2$, for similar fill-factors between reflective devices, the higher resolution tends to add more noise. This is explained by the fact that the number of cells is twice bigger to describe the same area of the image, each cells having intrinsic undesired effects, the resulting noise is proportional to the resolution.

The conclusion of this simulation is that the quadratic wavefront aberrations induced by lenses can be corrected using a spatial light modulator and that the GAEA (4094x2464) would give us the best result, even though the Pluto/Leto devices are also rendering acceptable outputs within the assumptions of our model.

Due to its mid-resolution, we are able to check the properties of the Pluto/Leto with its full physical resolution. We perform a simulation with a bigger discretization, namely 4094x4094 $\longrightarrow$ 15360x15360 leading to a device simulated with a resolution of 1920x1920 pixels, each of the cells modeled with 8x8 pixels. The table 4 shows the result for the higher discretization. One can notice the significant increase in the correlation rate. Within the assumptions of our model, this result could be expected in an experimental realization.

4094x4094	15360x15360
0.96370	0.99565

Table 4: Correlation rate for different discretizations, "worst case" simulation.

3 Optical realization of the Radon transform

The Radon transform is the set of projections of a function $f(x, y)$ to lines of orientation θ. The attractiveness of this transform is the existence of an inverse transform, allowing the reconstruction of objects starting from their projections. The Radon transform is widely used in computed tomography, image processing, pattern recognition and in motion detection.

3.1 The Radon transform

Let us consider a function $f(x, y) \in \mathbb{R}^2$ and a parametrized line at a distance r from the origin and forming an angle θ with the x-axis:

$$r = x\cos\theta + y\sin\theta. \tag{7}$$

The mathematical definition of the Radon transform R_f is given by:

$$R_f(r,\theta) = \iint_{-\infty}^{+\infty} f(x,y)\delta(x\cos\theta + y\sin\theta - r)dxdy \tag{8}$$

where δ is the Dirac function.

3.2 Parallel-Beam Geometry

One common way to realize the equation (8) is the parallel-beam geometry. For a given function $f(x, y)$ in Cartesian coordinates, we construct a hyperspace of lines $\mathcal{L}(r, \theta)$ defined by a distance r to the origin and an angle θ with the x-axis. The integral over each line gives the projection of the function $f(x, y)$ for a fixed angle, namely the Radon transform $R_f(r, \theta)$. The figure 7 pictures the parallel-beam geometry.

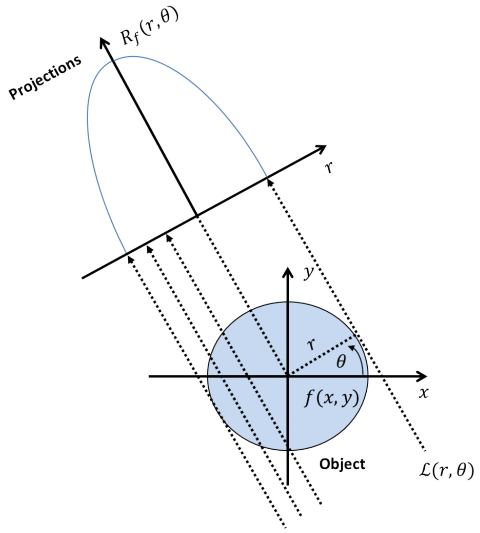

Figure 7: The parallel-beam geometry.

Octave and Matlab offer an built-in function ***radon()*** and the inverse ***iradon()***, based on the parallel-beam geometry. An image, representing a discretization of a signal $f(x, y)$, taken as an input is firstly padded then summed over each pixels for every lines. The next step is to increment the angle and repeat the approximation of the integral by a sum. The result is presented in a "polar-like" system of coordinates (r, θ). The inverse transform is implemented through the *filtered back projection* algorithm. The figure 8 shows the numerical computation of the Radon transform.

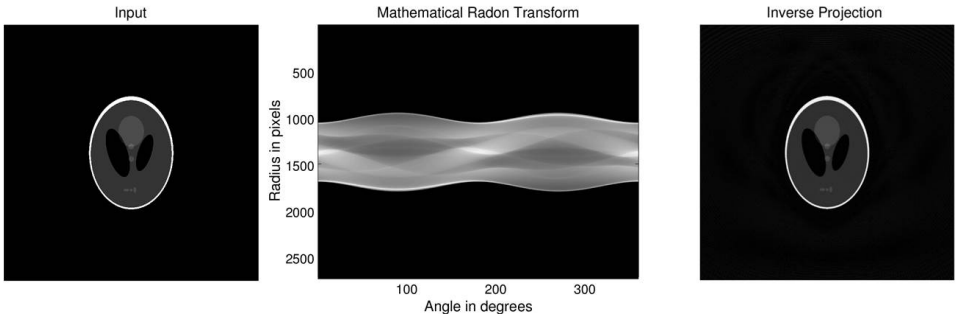

Figure 8: Numerical Radon transform and it's inverse computed from Octave's built-in function, resolution: 1920x1920, image size: 12.5mmx12.5mm, input size: 6 mm, left: input, middle: Radon transform, right: inverse transform.

3.3 Fourier Slice Theorem

Another common way to realize the Radon transform arises from a purely mathematical description. The Fourier Slice theorem, also known as the projection slice theorem, states that the two dimensional function $f(x, y)$ projected onto a one-dimensional line and Fourier-transformed is equivalent to the two-dimensional Fourier transform of the same function $f(x, y)$ sliced through its origin, where the slicing is parallel to the projection line.

This result allows us to rewrite equation (8). We first compute the one-dimensional radial Fourier transform of the Radon transform $\mathcal{F}_{(r)}[R_f](\frac{\sigma}{\lambda f}, \theta)$:

$$\mathcal{F}_{(r)}[R_f](\frac{\sigma}{\lambda f}, \theta) = \int_{-\infty}^{+\infty} R_f(r,\theta) e^{-\frac{2\pi i}{\lambda f}\sigma r} dr = \iiint_{-\infty}^{+\infty} f(x,y)\delta(xcos\theta + ysin\theta - r) e^{-\frac{2\pi i}{\lambda f}\sigma r} dxdydr$$

$$= \iint_{-\infty}^{+\infty} f(x,y) e^{-\frac{2\pi i}{\lambda f}\sigma[xcos\theta + ysin\theta]} dxdy = \mathcal{F}_{(x,y)}[f](\frac{\sigma}{\lambda f}cos\theta, \frac{\sigma}{\lambda f}sin\theta) \tag{9}$$

where λ is the wavelength and f the focal distance of a Fourier transforming lens. From equation (9), we deduce:

$$R_f(r,\theta) = \mathcal{F}^{-1}_{(\frac{\sigma}{\lambda f})} \mathcal{F}_{(x,y)}[f](rcos\theta, rsin\theta). \tag{10}$$

The equation (10) implies that the Radon transform is equivalent to applying a two-dimensional Fourier transform, performing a "polar-like" interpolation and then applying a one-dimensional inverse Fourier transform. The figure 9 shows the two polar interpolations that might be used in the Fourier sliced realization of the Radon transform. On the left, the standard polar interpolation defined as $(x, y) = (rcos\theta, rsin\theta)$. The problem with this representation lies in the fact that the parallel-beam geometry and thus the Radon transform intrinsically contains every informations twice. In order to recover the full Radon transform, one needs to translate the standard polar representation to the center and then double the information as if each mapping

radius was extended to the diagonals length of the input image. For simplicity, this process is shown in the real space on the figure 9, right. Although, following equation (10), the whole process is applied after the two-dimensional Fourier transform, therefore in the frequency space.

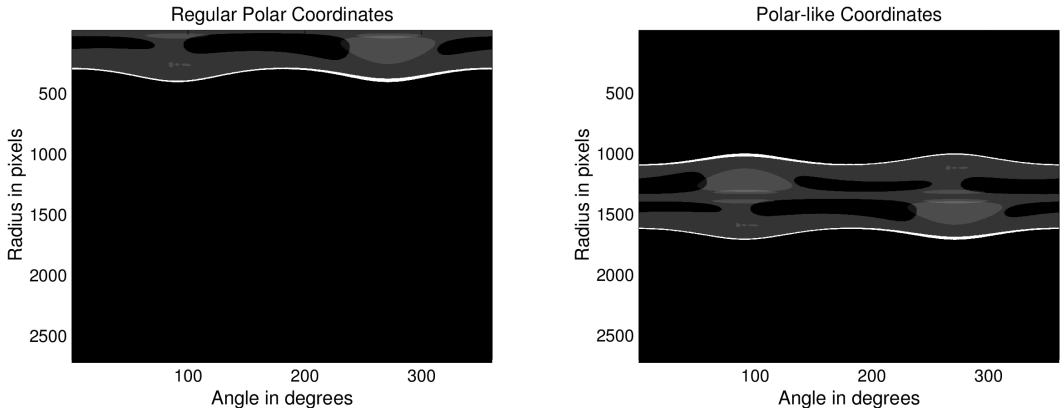

Figure 9: Projection onto polar coordinates, left : standard polar coordinate definition centered at the image center, right: polar coordinate to match the Radon transform

The figure 10 shows the Fourier slice realization of the Radon transform on the left and the inverse reconstruction on the right. The results are close to the ones of the parallel-beam realization: the correlation rate $corr2 \geq 0.99$. The artifacts appearing on the sides are due to the input size, a smaller input would yield to a better transformation. The non-bijectivity of the "polar-like" interpolation with the Cartesian domain could partially explain the artifacts. Indeed, due to the discretization and the finiteness of both domains, a polar interpolation is not bijective with a Cartesian domain and therefore every transformation is followed by a loss of information, especially at the borders. One way to overcome this issue is to zero-pad the image before the processing, unavoidably leading to a trade-off precision/computation time.

3.4 Optical realization of the Radon Transform

The optical realization of the Radon transform was first proposed by T. Ilovitsh *et al* [4]. Given a function $f(x, y)$, they design an optical processor able to solve equation (8). The whole process takes place in the Fourier domain where the filtering is realized using an optical element T defined as:

$$T(r, \theta) = \frac{e^{2\pi i \beta r \theta}}{r} \tag{11}$$

where (r, θ) is supposedly a standard polar domain and $\beta = 10^5$ is a parameter modulating the radius of the projections. The output is retrieved in Cartesian coordinates. The attractiveness of this optical element is the possibility to realize the phase element using a phase-only spatial light modulator. The left part of figure 11 shows the main result of the publication and is considered as the state of the art. The observation arising from the equation (11) is that a circular output is

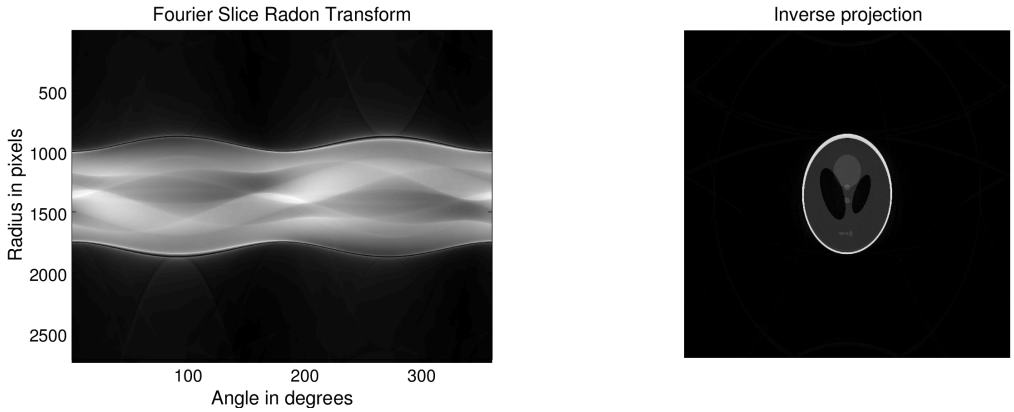

Figure 10: Fourier slice realization of the Radon transform , left : Radon transform, right: reconstruction using the Fourier slice inverse transformation.

generated using non polar-symmetric functions. A closer look at the phase element of $T(r, \theta)$ concludes that the multiplication between the radius r and the angle θ should generate spirals instead of circles. This hypothesis is verified through a simulation and the result is presented on the right part of figure 11. In order to retrieve the Radon transform, one should alter the angle θ in a non-physical way, by adding some arbitrary angles to the expression for example. This method is artificial and not generalizable, therefore, we propose a novel optical realization of the Radon transform.

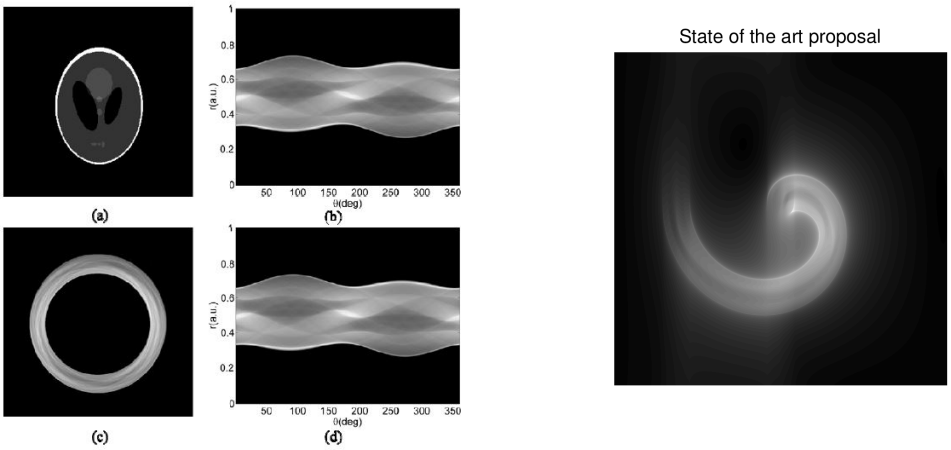

Figure 11: State of the art [4], left: (a) input, (b) the mathematical Radon transform, (c) the optical realization, (d) the optical realization processed in polar coordinates, right: our simulation attempt to reproduce the state of the art.

3.4.1 Theory

The main purpose of this section is to build a bridge between the raw mathematical definition and the engineering application of the Radon transform. Our leading intuition is that a physical realization might enhance the applicability, optically or numerically. The solution should satisfy two main constraints:

- The experimental realization is enabled using common optical processing tools (lenses, filters, sensors, ...).
- The output is obtained in a Cartesian referential and the different sets of coordinates involved in the mathematical definition are handled internally in a simple expression.

We define the Radon transform in a set of Cartesian coordinates (ξ, η) as:

$$R_f(\xi,\eta) = (f * t)(\xi,\eta) = \iint_{-\infty}^{+\infty} f(x,y)t(x-\xi, y-\eta)dxdy \tag{12}$$

where $*$ is the convolution operator and t is the impulse response of the optical processor.

For notation simplicity, the capital $T(\frac{u}{\lambda f}, \frac{v}{\lambda f}) = \mathcal{F}_{(x,y)}[t](\frac{u}{\lambda f}, \frac{v}{\lambda f})$ refers to the two dimensional Fourier transform of a function $t(x, y)$. The convolution theorem allows to rewrite equation (12) as :

$$R_f(\xi,\eta) = \frac{1}{(\lambda f)^2} \iint_{-\infty}^{+\infty} F(\frac{u}{\lambda f}, \frac{v}{\lambda f})T(\frac{u}{\lambda f}, \frac{v}{\lambda f})e^{\frac{2\pi i}{\lambda f}(u\xi+v\eta)}dudv \tag{13}$$

where $(\frac{u}{\lambda f}, \frac{v}{\lambda f})$ are the corresponding spatial frequencies in the Fourier domain. The equation (13) expresses an input signal f Fourier transformed, filtered by an optical element T and then inverse Fourier transformed. In order to satisfy our first constraint, the optical realization might be performed using a 4f-correlator.

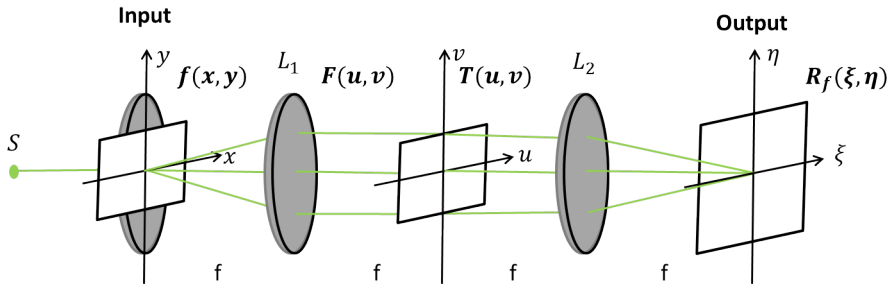

Figure 12: The 4f-correlator.

The figure 12 schemes the well-known 4f-correlator that allows to optically process a convolution of two functions. The input transparency $f(x, y)$, placed at a focal distance f on the object plane of the lens L_1, is illuminated with a monochromatic light source. The thin lens L_1 performs a two-dimensional Fourier transform

of our signal, which is then multiplied by an optical element on the image plane of L_1 (respectively the object plane of L_2). The outgoing signal is then Fourier transformed by the second lens L_2 and finally recorded in the image plane of L_2. The whole process describes a convolution of $(f * t)$. We want to compute T such that the output signal of our processor is the Radon transform of the signal f.

The figure 13 shows the set of coordinates (r, θ) used in the mathematical definition of the Radon transform following equation (7). The coordinate r represents the distance between the origin and a line over which the function $f(x, y)$ is integrated while θ modulates the inclination of it.

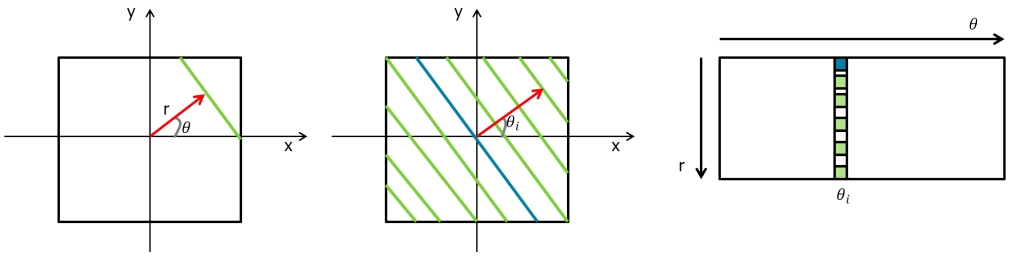

Figure 13: The Radon Transform, set of coordinate (r, θ).

The leading intuition to solve the problem is that a set of Cartesian coordinates $(\xi, \eta) = (r\cos\theta, r\sin\theta)$, representing the same hyperspace of lines, should recover the Radon transform as integrations over circles. From equation (12) and in order to satisfy the shift-invariance required by the convolution operator, we define:

$$t(x-\xi, y-\eta) = \delta(\pm(x-\xi)^2 \pm (y-\eta)^2 \pm \rho_0\sqrt{(x-\xi)^2 + (y-\eta)^2}) \qquad (14)$$

where ρ_0 is a constant parameter modulating the circle's radius. A more intuitive interpretation of equation (14) arises after a few algebraic manipulations:

$$t(x-\xi, y-\eta) = \int_0^{2\pi} \delta((x-\xi)\cos\theta + (y-\eta)\sin\theta - \rho_0)\delta(-x\sin\theta + y\cos\theta)d\theta. \quad (15)$$

The equation (15) has two equivalent interpretations, a geometrical and a mathematical one.

Geometrical interpretation

The figure 14 details the geometrical explanation behind equation (15). On the left, the first Dirac δ represents a line over which the function $f(x, y)$ is translated, the constant parameter ρ_0 shifts the distance of the line to the origin. In the middle, the second Dirac δ translates the function onto the perpendicular line passing through the origin. So far, the integration of a function $f(x, y)$ over space and both Dirac δ will translate the function to the intersection of both lines. Integrating over the angle will replicate the translations over a circle. From an optical point of view, the convolution with the impulse response $t(x-\xi, y-\eta)$ will project a source point emitting at the origin on a circle where the radius might be modulated by the

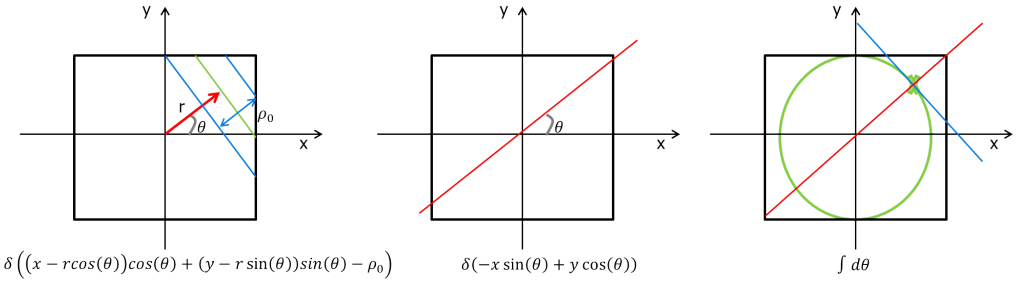

Figure 14: Geometrical interpretation

parameter ρ_0. From a numerical point of view, the constant parameter ρ_0 allows us to avoid the multiple definitions of Cartesian sets of coordinate, satisfying our second constraint and enabling a simple numerical implementation. The radius will *de facto* be matched.

Mathematical interpretation

From equation (12) and (15), we deduce

$$R_f(\xi,\eta) = \iint_{-\infty}^{+\infty} \int_{0}^{2\pi} f(x,y)\delta((x-\xi)\cos\theta + (y-\eta)\sin\theta - \rho_0)\delta(-x\sin\theta + y\cos\theta)d\theta dxdy$$

$$R_f(\xi,\eta) = \iint_{-\infty}^{+\infty} \int_{0}^{2\pi} f(x,y)\delta(x\cos\theta + y\sin\theta - \sqrt{\xi^2+\eta^2} - \rho_0)\frac{\delta(y - \frac{x\sin\theta}{\cos\theta})}{|\cos\theta|}d\theta dxdy$$

$$R_f(\xi,\eta) = \int_{-\infty}^{+\infty} \int_{0}^{2\pi} f(x, x\tan\theta)\delta(\pm x \pm \sqrt{\xi^2+\eta^2}\cos\theta \pm \rho_0\cos\theta)dxd\theta. \qquad (16)$$

The equation (16) can be interpreted as the integral of a function $f(x,y)$ over a line parametrized by $y = x\tan\theta$, which is exactly the mathematical definition of the Radon transform.

3.4.2 Analytical solution

In order to have a complete mathematical description, we need to compute the optical element $T(\frac{u}{\lambda f}, \frac{v}{\lambda f})$ performing the Radon transform in the experimental realization.

$$T(\frac{u}{\lambda f}, \frac{v}{\lambda f}) = \iint_{-\infty}^{+\infty} t(x-\xi, y-\eta)e^{\frac{2\pi i}{\lambda f}[(x-\xi)u + (y-\eta)v]}d(x-\xi)d(y-\eta)$$

$$T(\frac{u}{\lambda f},\frac{v}{\lambda f})=\iint_{-\infty}^{+\infty}\int_{0}^{2\pi}\delta((x-\xi)\cos\theta+(y-\eta)\sin\theta-\rho_0)\delta(-x\sin\theta+y\cos\theta) \times e^{\frac{2\pi i}{\lambda f}[(x-\xi)u+(y-\eta)v]}d\theta d(x-\xi)d(y-\eta). \tag{17}$$

We perform the canonical change of coordinate:

$$\begin{cases} t = & (x-\xi)\cos\theta + & (y-\eta)\sin\theta \\ s = & -(x-\xi)\sin\theta + & (y-\eta)\cos\theta \end{cases}$$

$$\begin{cases} (x-\xi) = & t\cos\theta - & s\sin\theta \\ (y-\eta) = & t\sin\theta + & s\cos\theta. \end{cases} \tag{18}$$

The equation (17) becomes

$$T(\frac{u}{\lambda f},\frac{v}{\lambda f})=\iint_{-\infty}^{+\infty}\int_{0}^{2\pi}\delta(t-\rho_0)\delta(s)e^{\frac{2\pi i}{\lambda f}t(u\cos\theta+v\sin\theta)}e^{\frac{2\pi i}{\lambda f}s(-u\sin\theta+v\cos\theta)}dtdsd\theta$$

$$T(\frac{u}{\lambda f},\frac{v}{\lambda f})=\int_{0}^{2\pi}e^{\frac{2\pi i}{\lambda f}\rho_0(u\cos(\theta)+v\sin\theta)}d\theta=\int_{0}^{2\pi}e^{\frac{2\pi i}{\lambda f}\rho_0\sqrt{u^2+v^2}cos(\theta-\alpha)}d\theta=2\pi I_0(\frac{2\pi i}{\lambda f}\rho_0\sqrt{u^2+v^2}) \tag{19}$$

where α is the angle between the vector $\vec{u}=(u,v)$ and the u-axis and

$$I_n(z)=\frac{1}{2\pi}\int_{0}^{2\pi}e^{zcos\theta}\cos(n\theta)d\theta \tag{20}$$

is the nth-order modified Bessel function of first kind.

Once replaced in the equation (13), the solution to the problem inspired by the 4f-correlator is given by

$$R_f(\xi,\eta)=\frac{2\pi}{(\lambda f)^2}\iint_{-\infty}^{+\infty}F(\frac{u}{\lambda f},\frac{v}{\lambda f})I_0(\frac{2\pi i}{\lambda f}\rho_0\sqrt{u^2+v^2})e^{\frac{2\pi i}{\lambda f}(u\xi+v\eta)}dudv. \tag{21}$$

3.4.3 Simulation

The purpose of the simulation is to confirm the mathematical development of the optical realization of the Radon transform. The figure 15 shows the simulation of the equation (21), on the left side the Cartesian realization, on the right side the processed output in polar representation. The correlation rate between the polar representation (Fig.15 right) and the parallel-beam implementation of the Radon transform(Fig.8 middle) is $corr2 > 0.99$.

A further investigation on the optical realization of the Radon transform might be done by comparing the realization with an analytical solution. We consider a circular input given by the function

$$f(x,y)=rect(\frac{\sqrt{x^2+y^2}}{2r_0}), rect(t)=\begin{cases} 1 & \text{if } |t|<\frac{1}{2} \\ 0 & \text{otherwise} \end{cases}. \tag{22}$$

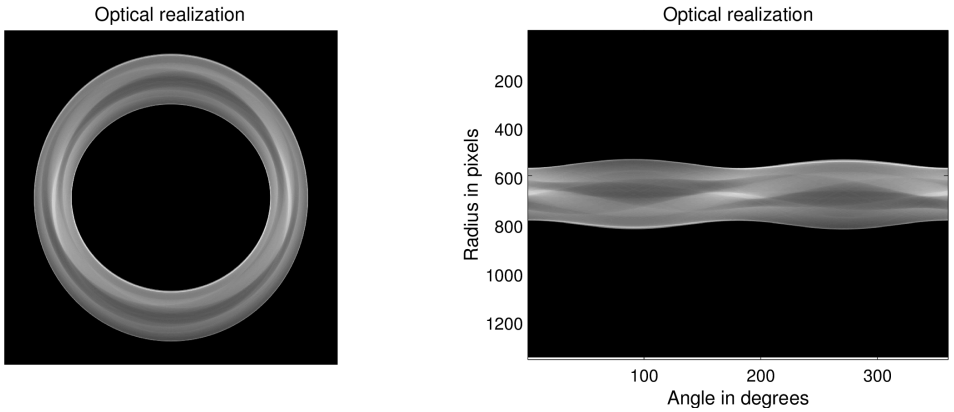

Figure 15: Optical realization of the Radon transform in Cartesian set of coordinates on the left, in polar set of coordinates on the right.

where r_0 is the radius of the input circle. A straightforward computation of equation (8) gives :

$$R_f(r,\theta) = 2\sqrt{r_0^2 - r^2}\, rect(\frac{r}{2r_0}). \tag{23}$$

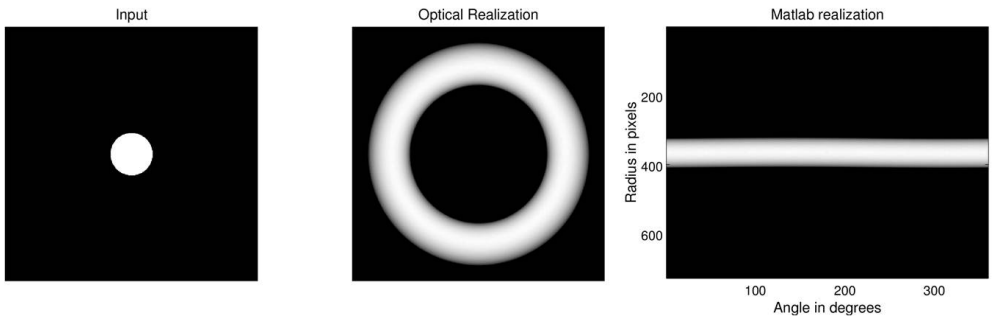

Figure 16: Analytical simulation, left: input, middle: optical Cartesian realization, right: Octave's polar realization.

The figure 16 shows on the left: the input given by (22), on the middle: the optical realization and on the right: the Octave realization of the Radon transform.

The figure 17 shows the comparison between the two different realizations with the analytical one given by equation (23). The first observation is that the Octave parallel-beam projection deviates from the analyitcal solution in two ways: a stepped approximation and an asymmetry with respect to the right side. Both effects are also present in the optical realization and might be explained by the discretization inherent to the ***radon()*** function and the Bessel function ***besseli()*** in Octave. One can also notice that the asymmetry present in the optical realization diverges from the left side. Increasing the discretization reduces the error but doesn't affect the asymmetries. Those asymmetries lead to artifacts in the inverse transformations between the Octave and optical realizations.

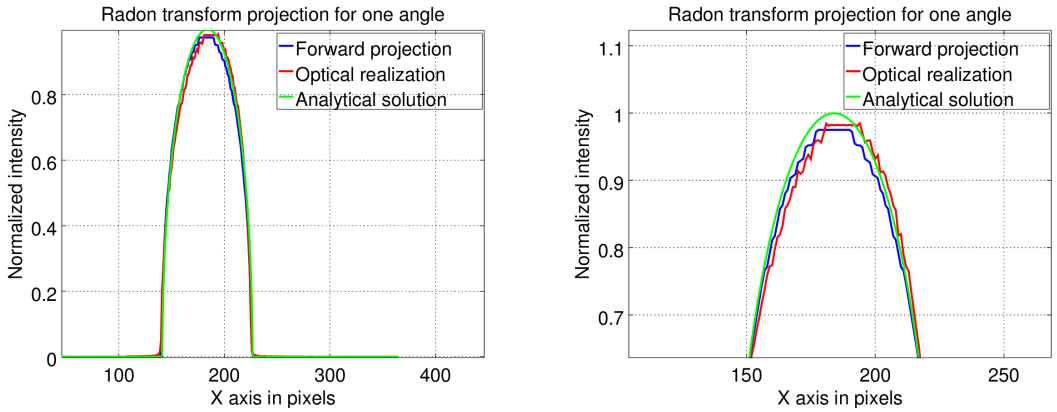

Figure 17: Three realizations comparison, analytical, optical and Octave parallel-beam realization, right: zoom.

A full description of the Radon transform must necessarily include the implementation of the inverse Radon transform. We build our model by analogy with the well-known *filtered back projection* algorithm. The main idea behind the *filtered back projection* is to run back-projections through the image in order to obtain a rough approximation to the original. The projections will interact constructively in regions that correspond to the emissive sources in the original image. A problem immediately apparent is the blurring (star-like artifacts) that occurs in other parts of the reconstructed image. One would expect that a high-pass filter might be used to eliminate the blurring. The optimal way to get rid of these patterns in the noiseless case is through a Ramp filter. By analogy, we apply two times the Radon transform in order to recover the blurry input image, and then filter it using a Ramp filter defined as:

$$H(\frac{u}{\lambda f}, \frac{v}{\lambda f})_{Ramp} = \frac{1}{\lambda f}\sqrt{u^2+v^2} \tag{24}$$

where $(\frac{u}{\lambda f}, \frac{v}{\lambda f})$ are the spatial frequencies in the Fourier domain.

The figure 18 shows on the left the parallel-beam back-projection, unfiltered and filtered, on the middle part, the optical inverse Radon transformation. Once the inverse transform computed, we can look at the cross recoveries, respectively the filtered back projection from the optical realization and the optical recovery from the parallel-beam projection. The figure 18 (right) shows the two different recoveries. On both recoveries, we see the same major artifacts arising from the asymmetry detailed in figure 17. Another possible explanation can come from the interpolation between Cartesian and polar coordinate systems. Our model is highly sensitive to the radius of projections modulated by ρ_0 in the optical realization. A better implementation of the modified Bessel function should be investigated in order to solve this issue.

3.5 Experimental realization proposal

We want to establish an experimental proof confirming the optical realization of the Radon transform. From the left side of equation (19), one can deduce that the

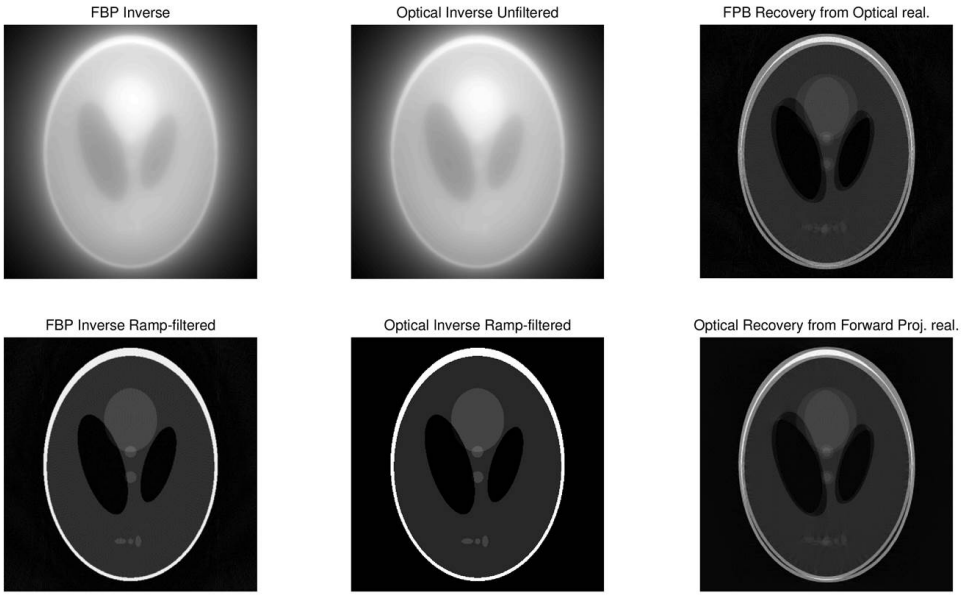

Figure 18: Inverse Radon transformation, left: parallel-beam back-projection and filtered reconstruction, middle: optical inverse realization and filtered reconstruction, right: cross recoveries.

modified Bessel function of first kind I_0 is entirely real valued, but from the right side it can be expected that some of the values are negative or larger than one. From an experimental point of view, a filter with negative values cannot be realized and a filter with values larger than one is a filter point-wisely creating light. None of this properties are realizable, especially not with a reflective *spatial light modulator*. Therefore, a way to overcome the problem is to realize the convolution with the signal $f(x, y)$ and the impulse response $t(x, y)$ in the object plane of the first lens. A convenient method to realize this convolution is the joint transform correlator.

3.5.1 The Joint Transform correlator

The joint transform correlator [5] is a method for performing complex filtering using a spatial carrier for encoding amplitude and phase information. Both the desired impulse response and the signal to be filtered are presented simultaneously during the recording process. Consider the recording in figure 19(a). Lens L_1, with focal length f, collimates the light from the point source S, with wavelength λ. This collimated light then illuminates a pair of transparencies residing in the same plane, h for the desired impulse response and g for the signal to be filtered. For simplicity this input is taken to be the front focal plane of the Fourier transforming lens L_2 (vignetting will be eliminated if the inputs are placed in contact with lens, rather than in front of it). The Fourier transform of the composite input appears in the rear focal plane of L_2, where the incident intensity is detected by a photographic medium, e.g. an image sensor.

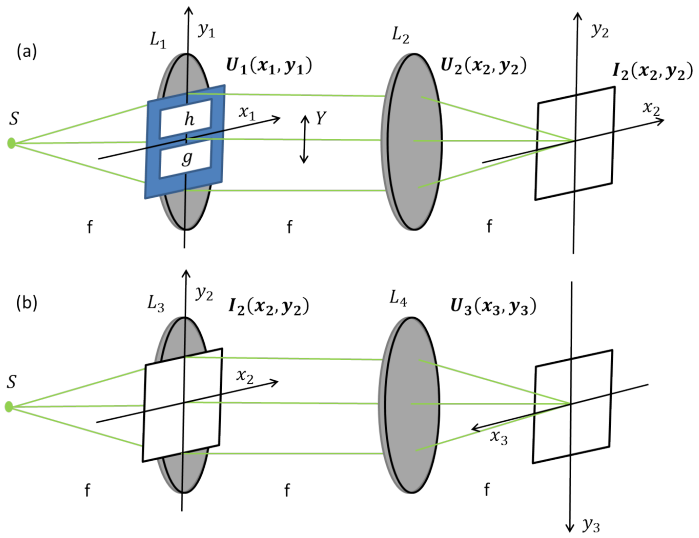

Figure 19: The joint transform correlator: (a) Recording the filter, (b) obtaining the filtered output.

The field transmitted through the front focal plane is given by

$$U_1(x_1, y_1) = h(x_1, y_1 - \frac{Y}{2}) + g(x_1, y_1 + \frac{Y}{2}) \tag{25}$$

where the separation between the centers of the two inputs is Y. In the image plane of the lens L_2 we find the Fourier transform of this field,

$$U_2(x_2, y_2) = \frac{1}{\lambda f} H\left(\frac{x_2}{\lambda f}, \frac{y_2}{\lambda f}\right) e^{\frac{-i\pi y_2 Y}{\lambda f}} + \frac{1}{\lambda f} G\left(\frac{x_2}{\lambda f}, \frac{y_2}{\lambda f}\right) e^{\frac{+i\pi y_2 Y}{\lambda f}} \tag{26}$$

where H, G are the Fourier transformations of h and g. Taking the square magnitude of this field, the incident intensity on the recording plane is found to be

$$\begin{aligned} I_2(x_2, y_2) = \frac{1}{\lambda^2 f^2} &\left[\left|H\left(\frac{x_2}{\lambda f}, \frac{y_2}{\lambda f}\right)\right|^2 + \left|G\left(\frac{x_2}{\lambda f}, \frac{y_2}{\lambda f}\right)\right|^2\right] \\ &+ \frac{1}{\lambda^2 f^2} H\left(\frac{x_2}{\lambda f}, \frac{y_2}{\lambda f}\right) G^*\left(\frac{x_2}{\lambda f}, \frac{y_2}{\lambda f}\right) e^{\frac{-i2\pi y_2 Y}{\lambda f}} \\ &+ \frac{1}{\lambda^2 f^2} H^*\left(\frac{x_2}{\lambda f}, \frac{y_2}{\lambda f}\right) G\left(\frac{x_2}{\lambda f}, \frac{y_2}{\lambda f}\right) e^{\frac{+i2\pi y_2 Y}{\lambda f}}. \end{aligned} \tag{27}$$

The transparency that results from this recording is assumed to have an amplitude transmittance proportional to the intensity that exposed it. After processing, this transparency, e.g. a transparent liquid crystal imaging device, is illuminated by collimated light and the the transmitted field is Fourier transformed by a lens L_4, assumed to have the same focal length f (see Fig. 19(b)). The field in the image

focal plane of L_4 is

$$\begin{aligned} U_3(x_3,y_3) = \frac{1}{\lambda f}\left[h(x_3,y_3) * h^*(-x_3,-y_3) + g(x_3,y_3) * g^*(-x_3,-y_3)\right] \\ + \frac{1}{\lambda f} h(x_3,y_3) * g^*(-x_3,-y_3) * \delta(x_3, y_3 - Y) \\ + \frac{1}{\lambda f} h(-x_3,-y_3) * g^*(x_3,y_3) * \delta(x_3, y_3 + Y). \end{aligned} \tag{28}$$

We can rewrite the 3rd and 4th term as

$$\begin{aligned} & h(x_3,y_3) * g^*(-x_3,-y_3) * \delta(x_3, y_3 - Y) \\ &= \iint_{-\infty}^{+\infty} h(\xi,\eta) g^*(\xi - x_3, \eta - y_3 + Y) d\xi d\eta \end{aligned} \tag{29}$$

and

$$\begin{aligned} & h^*(-x_3,-y_3) * g(x_3,y_3) * \delta(x_3, y_3 + Y) \\ &= \iint_{-\infty}^{+\infty} g(\xi,\eta) h^*(\xi - x_3, \eta - y_3 - Y) d\xi d\eta. \end{aligned} \tag{30}$$

Both of these expressions are cross-correlations between the functions g and h. One output is centered at coordinates $(0, -Y)$ and the other at coordinates $(0, Y)$.

In our case, both the impulse response h and the signal g are real valued. In order to recover the convolution as an output in (x_3, y_3), from equation (27), we subtract the two squared amplitudes before filtering the transparency in the second optical processor (Fig. 19(b)). This is done by passing each of the functions, separately, with a mirror image in the joint transform correlator.

3.5.2 Simulation

The joint transform correlator allows us to consider every element in the real space. The impulse response h as seen in figure 20(middle) is a circle. From an optical point of view, every point of the signal g will be projected on a circle through the convolution with the impulse response h leading to a sum over all the angles on the output. The implementation of the impulse response h is done by taking the Fourier transform of the optical element T defined by equation (19). Experimental requirements force us to resize $h(x, y) \in [0, 1]$. In order to generate the expected output (Fig. 20(right)), we perform the mathematical convolution $(g * h)$. The resizing induces artifacts in the output that will be expected in the output of the joint transform correlator.

The figure 21 shows the results of the joint transform correlator as it could be expected in an experimental realization. In order to generate the output $U_3(x_3, y_3)$, as suggested in equation (27), we perform the recording (Fig. 19(a)) three times: once with h and g, once with h and h and once with g and g. In the Fourier domain, we subtract the intensities from the two latter processes to the former one. We then take the resulting intensity and process it as prescribed in figure 19(b). The output is twice the convolution of the signal g and the impulse response h, both centered

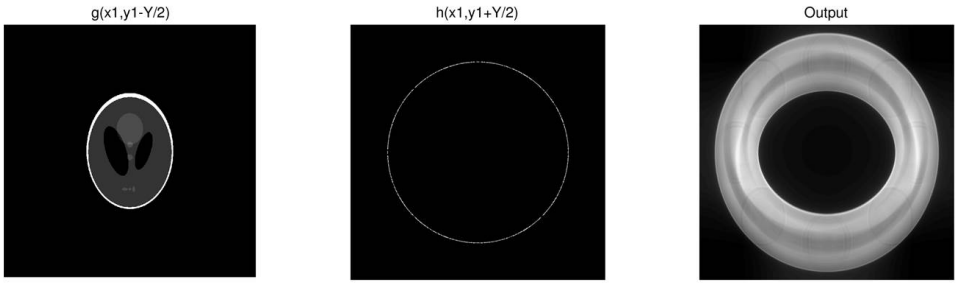

Figure 20: The joint transform correlator, left: the signal to be filtered g, middle: the impulse response h (contrasted), right: the expected output.

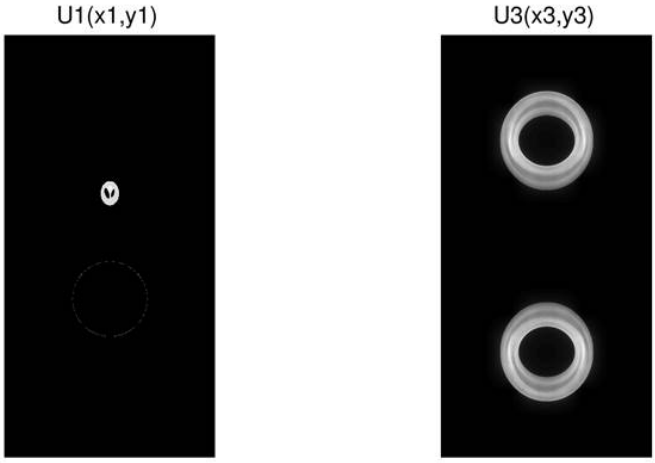

Figure 21: The joint transform correlator: optical realization of the Radon transform, left: $U_1(x_1, y_1)$ (contrasted), right: $U_3(x_3, y_3)$.

2 times further than the centers in the input $U_1(x_1, y_1)$, as predicted in equations (29) and (30).

The joint transform correlator has several other applications and some variants have been introduced in the literature. Placing an intensity spatial light modulator at the plane (x_2, y_2) or (x_3, y_3) allows to dynamically convolve, cross-correlate functions or add non-linearities leading to interesting applications in pattern recognition, security systems and super-resolution through compressive sensing. Depending on the application, the 4f-correlator and the joint transform correlator are interchangeable leading to interesting developments between optical and numerical processing.

4 Compressive sensing

We demonstrate the applicability of the optical Radon transform in a field where the parallel-beam geometry is commonly used: undersampled image reconstruction. The traditional approach of reconstructing signals or images from measured data follows the Shannon-Nyquist theorem, which states that the sampling rate must be twice the highest frequency. Similarly, the fundamental theorem of linear algebra suggests that the number of collected measurements of a discrete finite-dimensional signal should be at least the length of the signal in order to ensure reconstruction. The theory of compressive sensing provides a fundamentally new approach to data acquisition which overcomes this common wisdom. It predicts that certain signals or images can be recovered from what was previously believed to be highly incomplete measurements.

Compressive sensing is based on the empirical observation that many types of signals have a sparse representation in terms of a given basis. This means that the expansion has only a small number of significant terms.

4.1 Theoretical considerations

Let us first define the l_p-norm of a vector $x \in \mathbb{C}^N$

$$||x||_p := \left(\sum_{j=1}^{N} |x|^p \right)^{\frac{1}{p}}, 0 < p < \infty$$

$$||x||_\infty := \max_{j=1,..,N} |x_j|. \tag{31}$$

The support of a vector x is denoted $\text{supp}(x) = \{j : x_j \neq 0\}$, and

$$||x||_0 := |\text{supp}(x)|. \tag{32}$$

A vector x is called *k-sparse* if $||x||_0 \leq k$. Compressive sensing predicts that reconstruction from vastly undersampled measurement is possible. We define the measurement matrix $A \in \mathbb{C}^{m \times N}$ taking m linear measurements from a vector $x \in \mathbb{C}^N$. The measurement vector $y \in \mathbb{C}^m$ is given by:

$$y = Ax. \tag{33}$$

From equation (33) and in the case $m \ll N$, it is impossible to recover x from y since the linear system is highly underdetermined. However, if the assumption that the vector x is *k-sparse* is imposed, the underdetermination might be overcome.

The most intuitive approach for a recovery procedure is to search the sparsest vector x which is consistent with the measurement $y = Ax$. This leads to solving the l_0-*minimization problem*:

$$\min ||x||_0 \text{ subject to } Ax = y. \tag{34}$$

Unfortunately, an algorithm that solves the equation (34) for *any* matrix A and *any* y is necessarily computationally impossible (also called NP-hard problem). Two main alternatives have been proposed: convex relaxation leading to l_1-*minimization*- also called basis pursuit and greedy algorithms, such as various matching pursuits. A

detailed and complete survey of compressive sensing method and its algorithmic solutions has been done by M. Fornasier and H. Rauhut [6]. For simplicity and in order to compare our results to some state of the art research on the topic, we focus on the l_1-*minimization problem* through the method proposed by J.M Bioucas *et al*: TwIST [7].

4.2 TwIST algorithm

The two-step iterative shrinkage/thresholding algorithm, TwIST, is an open source algorithm for solving convex relaxation. We will only outline the main point of the method and the way we use it. Several applications such as denoising problems and compression problems are directly proposed in the defining paper [7]. The application to a computed tomography problem involving the Radon transform has been proposed by B.G. Chae *et al* [8] and will be considered as our state of the art point of comparison.

The image restoration is a classical linear inverse problem where starting from a measurement y we try to find the original image x (possibly noisy). The approach defines a solution as a minimizer of a convex objective function $f : \mathcal{X} \to \bar{\mathbb{R}} = [-\infty, +\infty]$, given by

$$f(x) = \frac{1}{2}||y - Ax||^2 + \lambda\Phi(x) \tag{35}$$

where $A : \mathcal{X} \to \mathcal{Y}$ is a linear direct operator, $\mathcal{X}$ and $\mathcal{Y}$ are real Hilbert spaces both with norm $||\cdot||$, Φ is a regularizer and λ a parameter. TwIST is an iterative algorithm represented as:

$$x^{k+1} = (1-\alpha)x^{k-1} + (\alpha - \beta)x^k + \beta\Gamma_\lambda(x^k) \tag{36}$$

$$\Gamma_\lambda(x) = \Phi_\lambda(x - A^{\mathrm{T}}(Ax - y)) \tag{37}$$

where α and β are parameters depending on the eigenvalues of the measurement matrix A. Let us define ξ_1 and ξ_m the minimal and maximal eigenvalue of A. Then κ is defined as $\frac{\xi_1}{\xi_m}$. The spectral radius ρ is given by

$$\rho = \frac{1 - \sqrt{\kappa}}{1 + \sqrt{\kappa}} < 1. \tag{38}$$

The performance of the algorithm is given by the two optimal parameters :

$$\alpha = \rho^2 + 1 \tag{39}$$

$$\beta = \frac{2\alpha}{\xi_1 + \xi_2}. \tag{40}$$

In order to specify equation (35), we need to focus our interest on the type of images we want to reconstruct. The Radon transform is widely used in Computed Tomography to reconstruct brain images from the projections. For practical reason, the signal's acquisition can't be made through a sparsifying operator such as a wavelet decomposition (very popular in compressive sensing). Therefore, we consider the l_2-norm as the norm of the Hilbert space. In order to overcome the sparsity problem arising, the Total Variation regularizer $||\nabla x||_1$ is considered because of the

empirical observation that most of the computed tomography images are sparse under gradient transform. The problem we solve using TwIST can be written as:

$$\min_x f(x) = \frac{1}{2}||Ax - y||_2^2 + \lambda||\nabla x||_1 \text{ subject to } Ax = y \tag{41}$$

where A is the optical realization of the Radon transform. One advantage of the TwIST algorithm is that we can use it with handle functions. Therefore, we define A as:

$$A = S \circ \mathcal{F}^{-1}[I_0 \circ \mathcal{F}[x]] \tag{42}$$

where I_0 is the 0-th order modified Bessel function of first kind, the operator $\circ$ is the element-wise (Hadamard) product and S is a stripping matrix corresponding to the measurements we take from a certain number of projections.

4.3 Simulation

We want to prove that the optical realization of the Radon transform leads to similar results as the state of the art [8]. Therefore we take the same intitial condition. The input image is the Shepp-Logan phantom with a resolution of 256x256 pixels. We take 32 projections from the Radon transform and reconstruct the input image using TwIST. The only difference is the way the measurement matrix A is generated. The state of the art uses the *parallel-beam geometry* and the *filtered back projection* while we use the optical realization of the Radon transform.

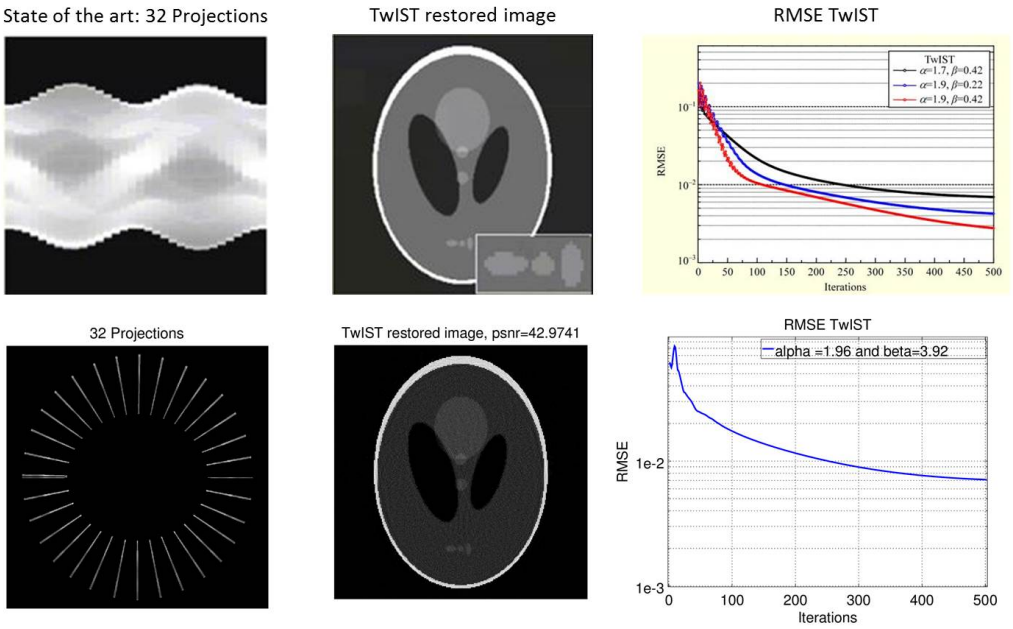

Figure 22: Image reconstruction using TwIST, upper part: state of the art results, lower part: optical realization results.

The figure 22 shows on the upper part the state of the art results and on the lower part the optical realization results. The left side details the 32 projections

taken from the Radon transform, in the middle the TwIST restored image and the right side represents the root mean square error (RMSE) directly provided by the TwIST algorithm with respect to the ideal image. The optical reconstruction uses a parameter $\lambda = 10^{-5}$ as a regularizer (see Eq.(35)). Since we use handle functions, we don't have an explicit access to the matrix A (which would be computationally extremely costly) and no access to the eigenvalues. Therefore, the parameters α and β are set to the defaults values suggested by the TwIST algorithm (namely $\xi_1 = 10^{-4}$ and $\xi_m = 1$). An improvement in the results could be investigated through the optimization of the parameters α and β. Nevertheless, considering the RMSE, one can conclude that the optical realization of the Radon transform leads to similar results as the ones from the parallel-beam geometry. The optical realization of the Radon transform can be used in image reconstruction, allowing a possible bridge between optical processing and numerical processing provided an improvement of the realization in the two fields. A further comparison can be made through the time required per iterations of the algorithm.

	256x256 32 Proj. [s]	256x256 64 Proj. [s]	512x512 32 Proj. [s]
Parallel-Beam	0.05	0.1	0.2
Optical Realization	0.2	0.2	0.8

Table 5: Parallel-Beam and Optical reconstruction with Matlab: time per iterations with respect to the resolution and the number of projections.

The table 5 shows the different times per iteration required by the algorithm with respect to the resolution and the number of projections. If N_{pix} is the total number of pixels and N_θ the number of projections, one can easily conclude that the complexity of the optical reconstruction is $\mathcal{O}(N_{pix})$ while the parallel-beam geometry complexity is $\mathcal{O}(N_{pix} \times N_\theta)$. One can notice that the time per iteration for the optical realization is 4 times bigger, this is due to the fact that the input is first zero-padded (256x256→1024x1024) before processing. This padding is made to ensure the one to one matching with the parallel-beam geometry and corresponds to the tuning of the parameter ρ_0 (see Eq.(19)). One way to overcome the padding issue is to tune the parameter ρ_0 is such a way that the circle of projections is contained in the initial resolution. Therefore, the conversion between the parallel-beam geometry and the optical realization would not be one to one anymore but in some kind of linear relation. This linear relation would obviously stay true in an experimental realization. Such a manipulation could lead to a significant improvement in the processing time, approximatively 16 times faster.

We also demonstrate the applicability of the realization on different sets of images. The figure 23 shows the different results in terms of peak signal to noise ratio (PSNR) for two different images. The quality of the reconstruction increases with the number of projections, as expected. The difference in the PSNR for the same number of projections is related to the sparsity of the signal under the Total Variation regularizer.

Further developments have been made by S. Evladov *et al* [9]. They solve the same reconstruction problem but using parallel-beam geometry with a direct access to the matrix A. Due to the computational cost of the matrix, they only generate the required rows for the forward projection via a method called Ordered

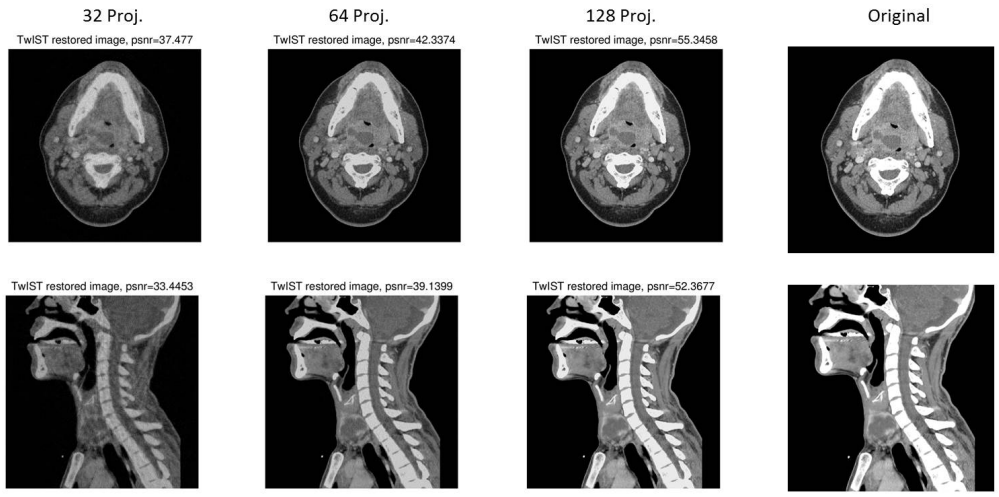

Figure 23: Optical Image reconstruction for different number of projections, upper: angiography, lower : head and neck.

Subset Estimation Maximization (OS-EM). They also provide a progressive method to reconstruct the input image by sampling with the golden angle with the TwIST algorithm. Although, due to the lack of quality criteria in their publication, it's hard to conclude if our implementation leads to any improvement concerning the reconstruction itself.

The figure 24 compares on the left the reconstruction of the Shepp-Logan phantom in terms of PSNR as a function of the projections, on the right, the state of the art [9]. Not having access to their input image, we only compare the behaviors of the reconstruction for two different image. The conclusion arising from the comparison, especially with the part (c), is that the reconstruction in the space domain of both images exhibits a similar tendency.

Finally, the optical realization of the Radon transform seems to behave as the parallel-beam geometry. Therefore, a further investigation should aim at improving the matching between the two methods in order to make them interchangeable, allowing a greater flexibility in optical and numerical processing.

5 Applications

Phase-only spatial light modulators, optical realization of the Radon transform and compressive sensing are the three main points we detailed with an application. So far, we couldn't link the optical realization of the Radon transform and the spatial light modulators or the spatial light modulators and the compressive sensing. Therefore, we introduce two experimentally realizable examples: an alternative proof of the optical Radon transform and the double random phase encoding.

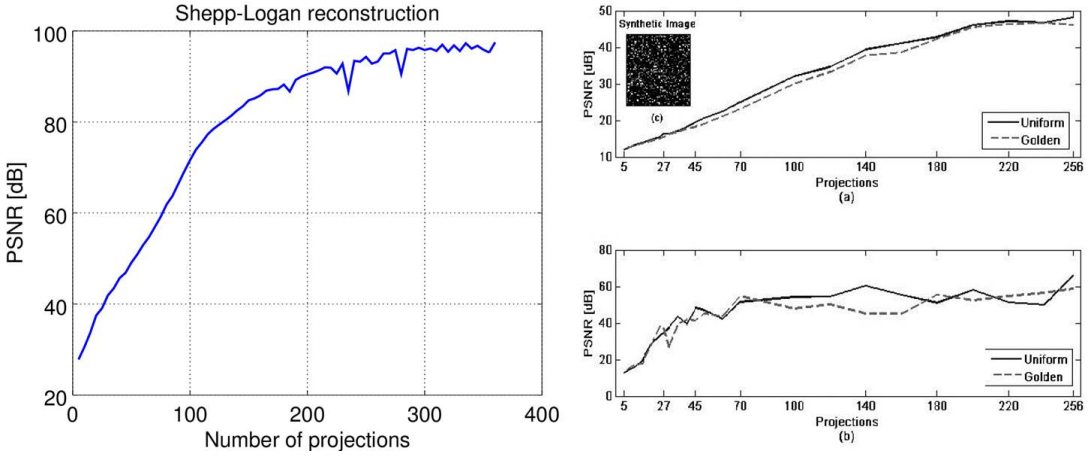

Figure 24: PSNR as number of projections, left: Shepp-Logan reconstruction in the space domain, right: state of the art [9] (a) reconstruction in the wavelet domain, (b) reconstruction in the space domain, (c) synthetic image as an input.

Alternative proof of the optical Radon transform

From equation (19), one can notice that the term to be integrated is a phase-element only. Approximating the integral by a sum we get

$$T(\frac{u}{\lambda f}, \frac{v}{\lambda f}) = \frac{1}{N} \sum_{\theta}^{2\pi} e^{\frac{2\pi i}{\lambda f} \rho_0 (u \cos\theta + v \sin\theta)} \tag{43}$$

where N is the total number of steps we use to discretize the domain $[0, 2\pi[$. The figure 25 shows the output of the simulation for $\theta = \frac{\pi}{2}$ and $\theta \in [\frac{\pi}{2}, \pi[$. As expected from the geometrical interpretation, the input image is projected on a circle where the radius is controlled by the parameter ρ_0. Once summed over a domain the Radon transform is recovered. One way to realize this experiment would be to generate each optical element one at a time and then to sum all the recorded pictures via post-processing. The simplest experimental setup is the 4f-correlator (Fig.12). Compactness could be achieved by using a single lens and a beam-splitter, taking advantage of the reflectiveness of the SLM. This way, lens aberrations can be corrected only for one lens and then multiplied to the optical element leading to a result close to the simulation. Agreeing results would be a proof that the optical realization of the Radon transform is related to the modified Bessel function of first kind. The advantage of the method is that the artifacts seen during the joint transform realization are suppressed and thus the recovery is more precise. Although, the clear trade-off precision/computational time appears and is directly related to the addressing time of the SLM device.

Double Random Phase Encoding

The double random phase encoding (DRPE) was first developed for optical security. Let us consider the figure 26. The optical system consists of two phase masks placed

Figure 25: Optical realization of the Radon transform for left: $\theta = \frac{\pi}{2}$, right: $\theta \in [\frac{\pi}{2}, \pi]$.

in the input and the Fourier plane. Let $f(x, y)$ be the signal we want to process. On its free propagation toward the Fourier transforming lens L_1, the signal is multiplied by a phase mask $e^{2\pi i p(x,y)}$ where $p(x, y)$ is an independently and identically distributed variable following an uniform distribution between [0,1]. On the plane (u, v) we recover

$$G(\frac{u}{\lambda f}, \frac{v}{\lambda f}) = \iint_{-\infty}^{+\infty} f(x, y) e^{2\pi i p(x,y)} e^{-\frac{2\pi i}{\lambda f}(xu+yv)} dxdy. \tag{44}$$

The transmitted field $G(\frac{u}{\lambda f}, \frac{v}{\lambda f})$ is then multiplied by a phase $e^{2\pi i b(\frac{u}{\lambda f}, \frac{v}{\lambda f})}$ where $b(\frac{u}{\lambda f}, \frac{v}{\lambda f})$ is also an independently and identically variable following an uniform distribution between [0,1]. Once the Fourier transforming lens L_2 is passed, we retrieve the output signal $g(\xi, \eta)$ in Cartesian coordinates :

$$g(\xi, \eta) = \frac{1}{(\lambda f)^2} \iint_{-\infty}^{+\infty} G(\frac{u}{\lambda f}, \frac{v}{\lambda f}) e^{2\pi i b(\frac{u}{\lambda f}, \frac{v}{\lambda f})} e^{\frac{2\pi i}{\lambda f}(u\xi+v\eta)} dudv. \tag{45}$$

The attractiveness of the whole process it that the output signal $g(\xi, \eta)$ is part of a single exposure compressive scheme. This is due to the fact that it implements a universal compressive sensing scheme. Indeed, it can be shown [10] that the DRPE behaves the same way as the Gaussian universal sensing operator. In a matrix representation, the first phase mask and the lens L_1 hold an inter-column statistical independence. Therefore $G(\frac{u}{\lambda f}, \frac{v}{\lambda f})$ is a de-correlated measurement of $f(x, y)$ in the space-domain. The second phase mask and the lens L_2 act in a similar manner but in the frequency domain. Finally, the whole process ensures that the output signal $g(\xi, \eta)$ holds a inter-row and inter-column statistical independence. In this manner, the output signal has the required properties to be fully reconstructed by compressive sensing algorithms, even if the signal is blurred or sub-sampled. Those interesting properties have been declined in a several number of applications such as super-resolution [10] or optical security [11].

The figure 27 presents an experimental setup to realize the DRPE. A realization might be done using a single reflective SLM. Taking advantage of the electrical

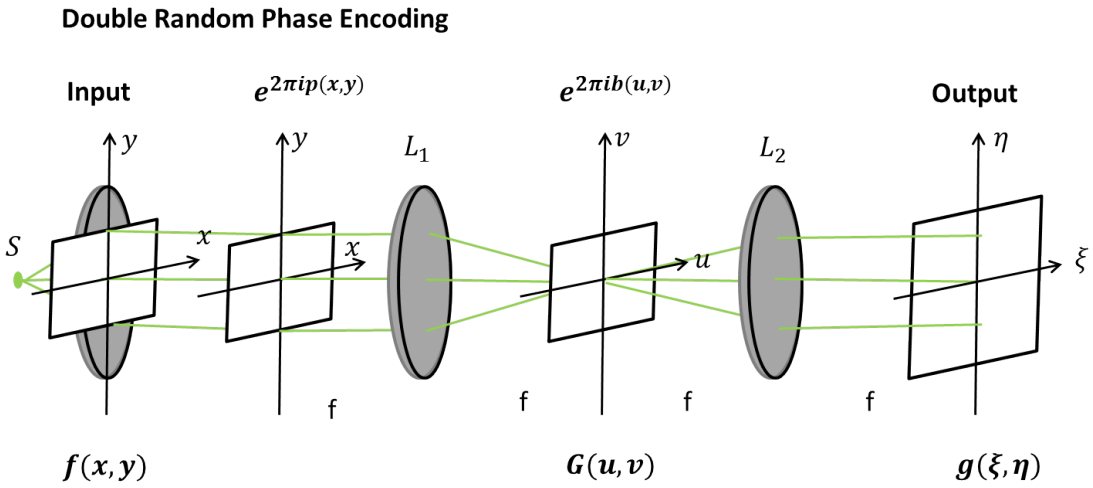

Figure 26: The double random phase encoding.

addressing property of the SLM, one can split the monitor in order to produce two different phase modulations. A suitable set of lenses should be used in order to keep a small angle of reflection and ensure the validity of the par-axial approximation. The output function recorded on the photographic medium has the compressive sensing properties required to perform an optimal reconstruction. The super-resolution theory states that the limiting resolution is the resolution of the optical processor itself and not the recorder, in this case, the resolution of the SLM. With a suitable algorithmic reconstruction, one should be able to retrieve the input image with the resolution of the SLM [10]. One can also note that the lens aberration is still possible to obtain better results.

6 Conclusion

Finally, the active field of image processing provides a lot of flexibility when it comes to solve challenging problems. The close bound between optical and numerical processing allows parallel improvements in both technologies leading to genuine solutions but also to enhancement in the way of thinking and solving problems.

Concerning the spatial light modulator, the technology is very promising and constantly growing. The wide range of applications arising from the dynamical character of the technology broadens the possibilities of image processing and announces the spatial light modulator as a strong candidate in forthcoming technologies. The combination with compressive sensing opens several prospects toward super-resolution, denoising, deblurring and various sorts of corrections that can strengthen the performance of an optical processor. A wider study should be accomplished on intensity modulators to understand their restrictions as wells as the possibilities it might offer in Fourier filtering.

Furthermore, the Radon transform and it's multiple expressions confirms its benefits in imaging. From the compressive sensing point of view, recovering an input

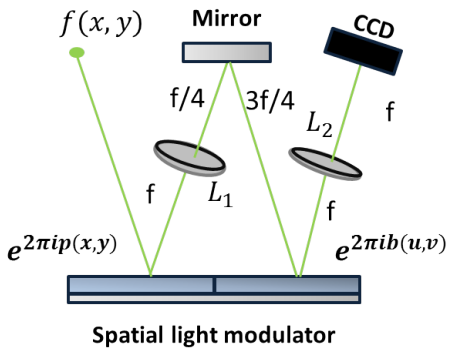

Figure 27: The experimental double random phase encoding.

image from a small number of projections expands the possibilities towards a lighter storage of informations and towards acquisition techniques. Regarding the expression itself, the possibility to compute it in Cartesian coordinates grants specific options in the sense of the Cartesian domain is naturally linked to numerical processing and a multitude of approaches can be used when it comes to manage noise or blurring. Further research should be conducted on the matching between the different realizations and on the possibility to apply the physically-inspired computation on the Radon transform in three or more dimensions as well as on other transforms such as the Funk transform and the Hough transform. Another topic to be investigated is the relationship between the optical realization and the Fourier-slice realization of the Radon transform. Recalling equation (10) and (21), the difference between the two realizations arises after the first two dimensional Fourier transform, suggesting that the filtering by the Bessel function followed by a two dimensional Fourier transformation is equivalent to performing a polar interpolation followed by a one dimensional Fourier transformation. This result opens up the possibility to perform a one dimensional radial Fourier transformation with an optical system.

References

[1] Hamamatsu, *"Phase Spatial Light Modulator LCOS-SLM"*, https://www.hamamatsu.com.

[2] HOLOEYE Photonics AG, *"http://holoeye.com"*, Berlin, Germany

[3] J.W. Goodman, *"Introduction to Fourier Optics"*, Roberts & Company, Third Edition, 2005.

[4] T. Ilovtish *et al*, *"Optical realization of the Radon transform"*, Optical society of America, 2014.

[5] C.J. Weaver and J.W.Goodman, *"A technique for optically convolving two functions"*, Appl. Opt., 5:1248-1249, 1966.

[6] M. Fornasier and H.Rauhut, *"Compressive sensing"*, Handbook of mathematical methods in imaging, 187-228, 2010.

[7] J.M Bioucas *et al*, *"A new TwIST: Two-Step Iterative Shrinkage/Thresholding algorithms for image restoration"*, IEEE, 2007.

[8] B. G. Chae and S. Lee, *"Sparse-view CT image recovery using Two-Step iterative shrinkage-thresholding algorithm"*, ETRI, 2015.

[9] S. Evladov *et al*, *"Progressive compressive imaging from Radon projections"*, Optical society of America, 2012.

[10] Y. Rivenson *et al*, *"Single exposure super-resolution compressive imaging by double phase encoding"*, Optical Society of Amercia, 2010.

[11] B. Javidi *et al*, *"Roadmap on optical security"*, IOPScience, 2016